

## Crosslinking and densification by plasma-enhanced molecular layer deposition for hermetic seal of flexible perovskite solar cells

Zhenyu Wang, Jintao Wang, Ze Li, Ziqiang Chen, Lianchao Shangguan, Siyu Fan, Yu Duan\*

*State Key Laboratory of Integrated Optoelectronics, College of Electronic Science and Engineering, Jilin University, Changchun 130012, China*



### ARTICLE INFO

**Keywords:**

Flexible thin film encapsulation  
Plasma-enhanced molecular layer deposition  
Crosslinking  
Stability  
Perovskite

### ABSTRACT

Flexible perovskite solar cells are new energy devices with a promising future due to their numerous advantages, such as high defect tolerance, strong solar absorption and low non-radiative carrier recombination rates. However, their operational stability is still an ongoing challenge during upgrading, and their inferior moisture corrosion resistance is still a major issue for better performances. Thin-film encapsulation could effectively enhance the operational stability of perovskite solar cells but obtaining encapsulation films with excellent barrier performance always come at the expense of poor flexibility. Therefore, the development of novel encapsulation materials with both barrier performance and flexibility is urgent for the compatibility of flexible applications. In this work, 'Plasma-Enhanced Molecular Layer Deposition' was used for the first time to prepare a highly cross-linked, densified flexible encapsulation material AlOC at 40 °C to break through the traditional technology. The resulting encapsulation material can be applied to flexible perovskite solar cells as a barrier film without any damage. The as-obtained encapsulation film exhibited a water vapor transmittance rate of  $1.44 \times 10^{-5} \text{ g m}^{-2} \text{ day}^{-1}$  and preserved 95 % of its initial barrier performance after 10,000 bends with a 3 mm bend radius. Such performance was the best among the reported thin-film encapsulation layers of flexible perovskite solar cells.

### 1. Introduction

Solar energy is a renewable and clean power source with irreplaceable advantages, such as sustainability, CO<sub>2</sub>-free emission, and 100 % inexhaustibility. Recently, metallic halide perovskite materials have drawn increasing attention in solar cells owing to their high defect tolerance, strong solar absorption, and low non-radiative carrier recombination rates [1,2]. So far, perovskite solar cells (PSCs) have made impressive progress in terms of power conversion efficiency (PCE), with significant enhancement from 3.8 % to 25.7 % [3]. Meanwhile, flexible perovskite solar cells (F-PSCs) are advantageous in terms of versatility, low cost, high specific energy, good compatibility with large-scale fabrication through roll-to-roll (R2R) processing and commercial viability [4,5]. However, the inferior operational stability of F-PSCs remains challenging, thereby inhibiting the technical feasibility and commercialization of photovoltaic technologies [6,7].

To solve these issues, tremendous efforts have been devoted to improve the stability against ambient moisture, such as compositional tuning and modification of perovskite solar cell stacks [8,9]. However,

these approaches did not eradicate the harmful aspect of moisture due to the incomplete isolation.

Barrier foil encapsulation is analogous to glass cover encapsulation, thereby can be used to protect flexible organic electronics. Examples of commonly used barrier foils are graphene, metal foil, and ultra-thin glass (under 50 μm thickness) [10,11]. However, the inevitable ultraviolet and thermal radiation during covering often damage devices, preventing the barrier foil from providing excellent flexibility.

Alternatively, thin-film encapsulation techniques, including chemical vapor deposition (CVD), atomic layer deposition (ALD), and sputtering can be utilized to prepare thin films with good density, as well as pinhole-free encapsulation to effectively protect organic electronics [12–14]. However, recent advances have demonstrated that PSCs are more sensitive to ambient temperature than organic light-emitting diodes (OLEDs) or organic photovoltaics (OPV). The defects induced by the low-temperature process often reduce the barrier performance of the encapsulation films to a large extent. For instance, Im et al. showed the existence of more defects in 21.5 nm-Al<sub>2</sub>O<sub>3</sub> films when grown at lower temperatures by thermal ALD. This provided additional permeation

\* Corresponding author.

E-mail addresses: [zyw20@mails.jlu.edu.cn](mailto:zyw20@mails.jlu.edu.cn) (Z. Wang), [jtwang@mails.cust.edu.cn](mailto:jtwang@mails.cust.edu.cn) (J. Wang), [lize19@mails.jlu.edu.cn](mailto:lize19@mails.jlu.edu.cn) (Z. Li), [2020100176@mails.cust.edu.cn](mailto:2020100176@mails.cust.edu.cn) (Z. Chen), [sglz20@mails.jlu.edu.cn](mailto:sglz20@mails.jlu.edu.cn) (L. Shangguan), [fansy21@mails.jlu.edu.cn](mailto:fansy21@mails.jlu.edu.cn) (S. Fan), [duanyu@jlu.edu.cn](mailto:duanyu@jlu.edu.cn) (Y. Duan).

paths for moisture, resulting in a sharp increase in water vapor transmission rate (WVTR) by two orders of magnitude ( $10^{-3}$  g m<sup>-2</sup> day<sup>-1</sup> @ 120 °C to  $10^{-1}$  g m<sup>-2</sup> day<sup>-1</sup> @ 60 °C) [15]. Similarly, we found that 45 nm-Al<sub>2</sub>O<sub>3</sub> film prepared by thermal ALD at 50 °C had increased WVTR by two orders of magnitude than at 110 °C ( $10^{-4}$  g m<sup>-2</sup> day<sup>-1</sup> @ 110 °C to  $10^{-2}$  g m<sup>-2</sup> day<sup>-1</sup> @ 50 °C) [16]. In addition, the inherent properties of resulting inorganic films prevented their flexible applications. In a recent study, Chang et al. prepared 50 nm Al<sub>2</sub>O<sub>3</sub> film via thermal ALD at 80 °C for using in the encapsulation of PSCs. The films showed excellent barrier performances with a WVTR of  $9.0 \times 10^{-4}$  g m<sup>-2</sup> day<sup>-1</sup>. However, the mechanical properties of WVTR based on Al<sub>2</sub>O<sub>3</sub> increased by 2.3-fold after bending 1000 times at a bending radius of 13 mm, indicating a great sacrifice in flexibility [17]. For this reason, organic/inorganic laminate structures have widely been explored due to their excellent flexibility. For example, Chen et al. inserted well wettable PDMS layer into Al<sub>2</sub>O<sub>3</sub> barrier film to extend the permeation pathway and increase the critical tensile strain of nanolaminates. The obtained multilayered barrier structure maintained a low WVTR of  $2.63 \times 10^{-3}$  g m<sup>-2</sup> day<sup>-1</sup> under 60 °C and 90 % relative humidity after a bending test with a radius of 5 mm [18]. Park et al. inserted alucone film prepared by molecular layer deposition (MLD) into the ALD-Al<sub>2</sub>O<sub>3</sub> monolayer to improve the mechanical properties. The flexibility of the resulting 60 nm-ALD/MLD laminated structure significantly improved when compared to the Al<sub>2</sub>O<sub>3</sub> monolayer. In 3 mm bending radius for 5000 repetitions, the WVTR of 60 nm-Al<sub>2</sub>O<sub>3</sub> increased by 19.7-fold, while that of 1.5 dyads-Al<sub>2</sub>O<sub>3</sub>/Alucone rose by only 13.4-fold, indicating that alucone could effectively improve the flexibility. Furthermore, the flexibility significantly improved as a function of the number of dyads, while WVTR improvement of 4.5 dyads-Al<sub>2</sub>O<sub>3</sub>/Alucone was further reduced by 7.4-fold [19]. However, such performance is still insufficient for future flexible encapsulation needs and the development of innovative encapsulation processes with both barrier performance and flexibility at low temperatures is urgent.

Herein, an organic-inorganic hybrid material (Al<sub>x</sub>O<sub>y</sub>C<sub>z</sub>) was grown by plasma-enhanced MLD (PEMLD) for the encapsulation of F-PSCs. The encapsulation process was performed at a low temperature of 40 °C without damage to the device. The oxidation of carbon backbone in ethylene glycol (EG) by O plasma provided additional reactive sites for trimethylaluminum (TMA), and the resulting O-Al-O bonds cross-link otherwise parallel and independent C-C backbone, significantly improved barrier performance due to the reduction of moisture permeation paths. Moreover, the cross-linked structure enhanced the film toughness and maximized the flexibility of the organic backbone. The optimal encapsulation film prepared by PEMLD exhibited excellent barrier performance with a WVTR of  $1.44 \times 10^{-5}$  g m<sup>-2</sup> day<sup>-1</sup>, as well as preserved 95 % of the initial barrier performance after 10,000 bends with a 3 mm bending radius due to its potent crack-inhibition characteristics. To the best of our knowledge, MLD has not yet been adopted in F-PSCs encapsulation and our report is the first of its kind. In sum, the proposed PEMLD represented a breakthrough and innovation in materials, processes, and structures of flexible thin-film encapsulation technology.

## 2. Experimental methods

### 2.1. Materials

SnO<sub>2</sub> colloidal solution (15 % in water) and Lead iodide beads (PbI<sub>2</sub>, 99.999 %) were purchased from Alfa Aesar. Dimethylsulfoxide (DMSO, 99.7 %), dimethylformamide (DMF, 99.8 %), isopropanol (IPA, 99.7 %), acetone (99.9 %), chlorobenzene (CB, 99.8%), 4-tert-butyl pyridine (98 %), acetonitrile (ACN, 99.8 %), lithium bis(trifluoromethanesulfonyl) imide (Li-TFSI, 99.95 %), AIBN (98 %), and dimethyl itaconate (99 %) were purchased from Sigma-Aldrich. Methylammonium iodide (MAI) and Formamidine iodide (FAI) were obtained from GreatCell Solar Materials (Australia). Spiro-oMeTAD (99.8 %) and methylammonium

chloride (MACl) were provided by Xi'an Polymer Light Technology in China. All the materials were used as received without further purification.

### 2.2. Fabrication of TFE

The pressure in the reaction chamber was maintained at 0.25 Torr during the process, and high-purity Ar (99.999 %) with a flow rate of 100 sccm was adopted as the carrier gas and cleaning gas of the precursor. First, PEALD-Al<sub>2</sub>O<sub>3</sub>: Trimethyl aluminum (TMA, 99.9999 %) and O plasma were used as the aluminum precursor and oxidizer of PEALD-Al<sub>2</sub>O<sub>3</sub>, respectively. Note that TMA was maintained at room temperature, and O plasma was generated by 15 sccm O<sub>2</sub> (99.999 %) under a radio frequency power of 100 W throughout the PEALD process. The substrate temperature was set to 40 °C, and typical process parameters for the growth of PEALD-Al<sub>2</sub>O<sub>3</sub> consisted of O plasma pulse of 10 s, O plasma purge of 100 s, TMA pulse of 0.04 s, and TMA purge of 100 s. Second, MLD-alucone: TMA and ethylene glycol (EG, 99.8 %) were used as the aluminum precursor and oxidizer of MLD-alucone, respectively. The TMA was maintained at room temperature, while the EG was heated to 80 °C for better reactivity. The substrate temperature was set to 40 °C or 80 °C as required, and typical process parameters for the growth of MLD-alucone consisted of TMA pulse of 0.04 s, TMA purge of 100 s, EG pulse of 4 s, and EG purge of 120 s. Third, PEMLD-ALCO: TMA, EG, and O plasma were used as the aluminum precursor, oxidizer A, and oxidizer B of PEMLD-ALCO, respectively. The O plasma was generated by 15 sccm O<sub>2</sub> (99.999 %) under a radio frequency power of 100 W. The TMA was maintained at room temperature, while EG was heated to 80 °C for better reactivity. The substrate temperature was set to 40 °C or 80 °C as required, and typical process parameters for the growth of PEMLD-ALCO consisted of TMA pulse of 0.04 s, TMA purge of 100 s, EG pulse of 4 s, EG purge of 120 s, O plasma pulse of 5 s, and O plasma purge of 100 s. For O plasma self-saturating surface reaction, the pulse time of O plasma was also set to 1, 3, and 11 s, respectively.

### 2.3. Fabrication of F-PSCs

PEN/ITO substrates were firstly cleaned with detergent, deionized water, acetone, and IPA for 30 min in sequence. The nitrogen gun and UV-ozone were used for drying and removal of organic residue of such substrates, respectively. SnO<sub>2</sub> (0.2 mL) colloidal solution was diluted in deionized water (1.2 mL) and the resulting mixture was spin-coated on the cleaned flexible substrates at the rate of 3000 rpm for 30 s, followed by annealing at 150 °C for 30 min under ambient environment to yield uniform SnO<sub>2</sub> films. Next, the substrates were treated by the UV-ozone for another 10 min followed by cooling down to ambient temperature and transferred into the glovebox to prepare the perovskite films. PbI<sub>2</sub> (1.5 mmol) was dissolved in DMF with DMSO as an additive (volume ratio of DMF:DMSO = 9:1), and then spin-coated on PEN/ITO/SnO<sub>2</sub> at the rate of 1500 rpm for 30 s, followed by annealing at 90 °C for 5 min. FAI (90 mg), MAI (6.39 mg), and MACl (9 mg) were dissolved in IPA (1 mL) and then spin-coated on PbI<sub>2</sub> films at the rate of 2000 rpm for 30 s, followed by annealing at 150 °C for 12 min in air environment outside the glovebox. The substrates were again transferred into glovebox to prepare the spiro-oMeTAD film after cooling down to ambient temperature. Spiro-oMeTAD solution (40 μL) consisting of 72.3 mg spiro-oMeTAD, 28.8 μL of 4-tert-butyl pyridine, and 17.5 μL of Li-TFSI solution (520 mg mL<sup>-1</sup> Li-TFSI in acetonitrile) in 1 mL of chlorobenzene was then spin-coated on perovskite films at the rate of 3000 rpm for 30 s. Finally, 100 nm-thick Ag was thermally evaporated at an evaporation rate of 0.5 Å s<sup>-1</sup>.

### 2.4. Film characterization

*In-situ* quartz crystal microbalance (QCM) (SQM160, INFICON) and *in-situ* quadrupole mass spectrometry (QMS) measurements were

simultaneously implemented during film growth of PEALD, PEMLD and MLD process to detect evolutions in film mass and by-product in chamber. PEMLD-AlCO and MLD-alucone were deposited on KBr tablets for 300 cycles then subjected to Fourier transform infrared spectroscopy (FTIR, PerkinElmer Spectrum One) analysis to determine the chemical components based on the bond bending and stretching vibration. In the meantime, X-ray photoelectron spectroscopy (XPS, Thermo ESCALab 250 analyzer) analysis was adopted under a constant energy mode to both films grown on  $10 \times 10$  mm silicon wafers for 300 cycles to determine the elemental composition, elemental ratio (C, O, Al) and chemical bond structures (C—O bonds, O—C—O bonds and C—C bonds). Scanning electron microscopy and energy dispersive X-ray spectroscopy was also used to determine elemental ratio of films. To obtain film thickness and refractive indexes, the films grown on  $25 \times 25$  mm silicon wafers were measured at three ellipsometry angles ( $55^\circ$ ,  $65^\circ$ , and  $75^\circ$ ) via variable-angle spectroscopic ellipsometry (J. A. Woollam) measurement, and the experimental data were fitted based on Cauchy model. Optical microscopy and SEM (JSM-7500F, JEOL; accelerating voltage of 5 kV) are used for macroscopic judgment and microscopic analysis of film cracking, respectively. The optical transmittance of films in the visible wavelength was measured by UV-vis-IR spectrophotometer (UV3600, SHIMADZU). Atomic force microscopy (AFM, using ICON-PT, Bruker) was used to analyze surface topography under a tapping mode. The crystallographic structure of  $\text{FA}_x\text{MA}_{1-x}\text{PbI}_3$  before and after encapsulation was determined by X-ray diffraction analysis (XRD, model D/max 2400). PEN was used as a flexible substrate in bending test, PEN/TFE was placed in the three-axis bending equipment (Folding Test System FT-300, Fstar) to simulate the real bending situation, the bending radius was set to 1–3 mm according to the demand, the bending speed was  $180^\circ/\text{s}^{-1}$ , and the duration of the bending state was 1 s. Electrical and optical calcium corrosion testing was used for the detection of WVTR and moisture permeation paths of barrier film, respectively. The calcium film with a thickness of 200 nm was evaporated to a  $10 \times 2.25$  mm region, and the Al film with a thickness of 100 nm was deposited on both sides of the calcium film as contact electrodes. Agilent B2902A Precision Source (Agilent Technologies, Inc., Santa Clara, CA, USA) was used to measure the electrical conductance ( $1/R$ ) of the calcium film under 80 % relative humidity at  $30^\circ\text{C}$ . The WVTR was calculated according to the following Equation:

$$\text{WVTR} = -n \cdot M_{(\text{H}_2\text{O})}/M_{(\text{Ca})} \cdot \delta_{(\text{Ca})} \cdot \rho_{(\text{Ca})} \cdot L/b \cdot d_{(1/R)}/d_{(t)}$$

where  $n$  is a stoichiometric coefficient ( $n = 2$  for  $\text{H}_2\text{O}$ ).  $M_{(\text{H}_2\text{O})}$  and  $M_{(\text{Ca})}$  correspond to the molar masses of  $\text{H}_2\text{O}$  and Ca, respectively.  $\delta_{(\text{Ca})}$  refers to Ca resistivity, and  $\rho_{(\text{Ca})}$  is the Ca density.  $L$  and  $b$  are the length and width of the Ca active layer, respectively.  $(1/R)$  represents the conductance measured during testing. A charge-coupled image sensor (acA1920-50gm, Basler) was used to obtain grayscale images of calcium film during the corrosion process.

## 2.5. Device characterization

The current-voltage (J-V) characteristics of the devices were studied by a digital source meter (Keithley model 2400, USA) under an ambient environment. A 450 W Xenon lamp (Oriel, USA) was employed as the light source for J-V measurements. The spectral output of the lamp was filtered by a Schott K113 Tampax sunlight filter (Präzisions Glas & Optik GmbH, Germany) to reduce the mismatch between the simulated and actual solar spectrum to less than 2 %. The photo-active area of  $0.1 \text{ cm}^2$  was used as dark-colored metal mask.

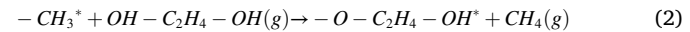
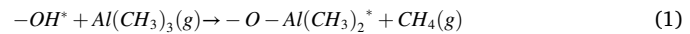
## 3. Results and discussion

In this section, all sample preparation processes were done in a super-clean laboratory. MLD-alucone or plasma-enhanced ALD (PEALD)- $\text{Al}_2\text{O}_3$  were grown by alternating pulses of TMA and EG or TMA

and O Plasma, respectively, and PEMLD-AlCO was grown by sequential pulses of EG, O plasma and TMA. The typical process parameters have been described in detail in the Experimental Section.

### 3.1. Low-temperature steric hindrance in MLD technology

Analogous to ALD process, MLD could precisely form films via alternating pulses. In MLD, the surface reaction self-limiting properties enable the growth of single molecular layers as units, commonly used for growing organic or organic-inorganic hybrid films. However, the distinctive convention of MLD technique relies on the precursors containing longer molecular chains than in ALD, resulting in potential steric hindrance. Eqs. (1) and (2) represent two surface half-reactions of alucone films grown via MLD, where the chemical bonds exposed on the surface of the substrate are marked with a “ $*$ ” [20].



As shown in Fig. 1a, the alucone film was grown by MLD at  $40^\circ\text{C}$  and  $80^\circ\text{C}$ , respectively. The growth process was monitored in real-time by *in-situ* quartz crystal microbalance (QCM). As can be seen, an obvious negative mass gain occurred after EG injection at  $40^\circ\text{C}$ , indicating that physically adsorbed EG molecules on the substrate surface underwent desorption during the purge process [21]. Inversely, the surface half-reaction potential barrier between EG and  $-\text{CH}_3$  declined at  $80^\circ\text{C}$ , while the chemisorption ratio increased. As a result, no significant negative mass gain was noticed after EG injection, indicating  $80^\circ\text{C}$  as a mild temperature for the growth of alucone [22]. By contrast, no negative mass gain occurred at both temperatures using TMA due to the high reactivity of TMA ensuring excellent surface chemisorption.

Consequently, growth depict can be divided into two categories. The first consisted of the unsaturated chemistry caused by shading of  $-\text{CH}_3$  from the chemisorbed EG molecules, called structural steric hindrance (Fig. 1c) [23]. This step can be described as self-limiting. Similarly, specific proportions of EG molecules were physically adsorbed on the substrate surface through van der Waals forces, obscuring the  $-\text{CH}_3$  beneath them and leading to unsaturated chemistry during the injection of EG to cause a steric hindrance. However, such EG molecules bound to the substrate by physisorption might be desorbed during the purge process, leading to the second step called transient steric hindrance (Fig. 1d) [21]. The occurrence of this second step was particularly severe at low temperatures. In addition, the  $-\text{OH}$  at both ends of EG molecular could react with the active sites  $-\text{CH}_3$  exposed on the substrate surface, which was called “double reaction” of homobifunctional precursors [24]. The  $-\text{OH}$  originally used for the next surface reaction with TMA was consumed during the double reaction process, therefore, the density of active sites  $-\text{OH}$  exposed on the substrate surface decreased. Under the influence of steric hindrance and “double reaction”, alucone exhibited a sparse and porous morphology with an inferior barrier performance. As depicted in Fig. S1, the WVTR value of 50 nm-alucone grown at  $80^\circ\text{C}$  was estimated to only  $1.65 \times 10^{-3} \text{ g m}^{-2} \text{ day}^{-1}$ . As the growth temperature further reduced to  $40^\circ\text{C}$ , the transient steric hindrance became more pronounced with numerous moisture permeation paths generated inside the alucone, resulting in a WVTR of  $3.78 \times 10^{-3} \text{ g m}^{-2} \text{ day}^{-1}$ . This would drastically affect the applications of MLD in the field of F-PSCs encapsulation.

### 3.2. Crosslinking and densification from PEMLD

As mentioned above, the self-limiting nature of structural steric hindrance created by the EG molecules limited the chemical reaction between EG or molecules with larger spatial volume and  $-\text{CH}_3$ . Accordingly, O plasma was first injected at the pulse of 5 s when EG became fully desorbed and then followed by a TMA pulse. After sufficient cleaning of EG, the  $-\text{CH}_3$  active site, originally obscured, became

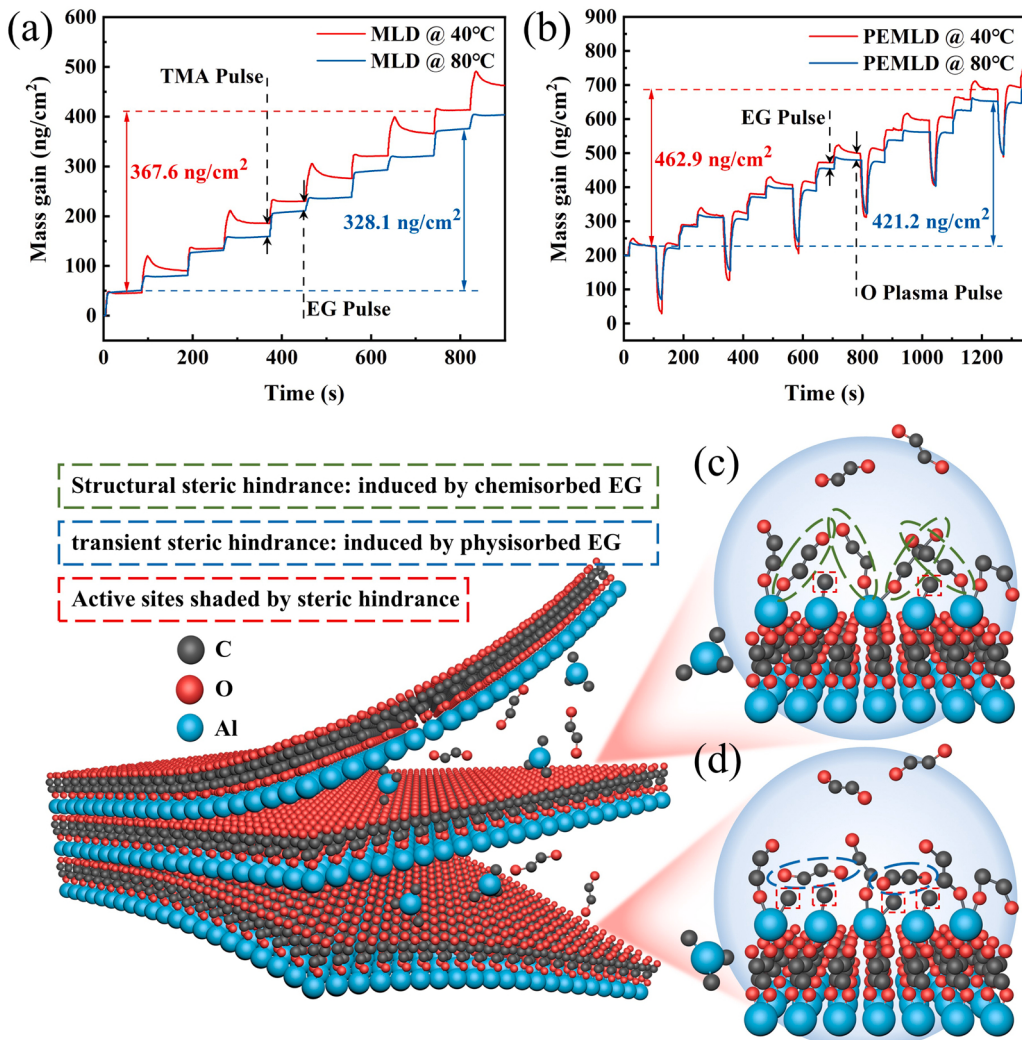
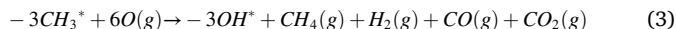


**Fig. 1.** Mass gain curve converted by *in-situ* QCM at 40 °C and 80 °C of (a) alucone grown by MLD and (b) AlCO grown by PEMLD. Schematic diagram of (c) structural steric hindrance and (d) transient steric hindrance.

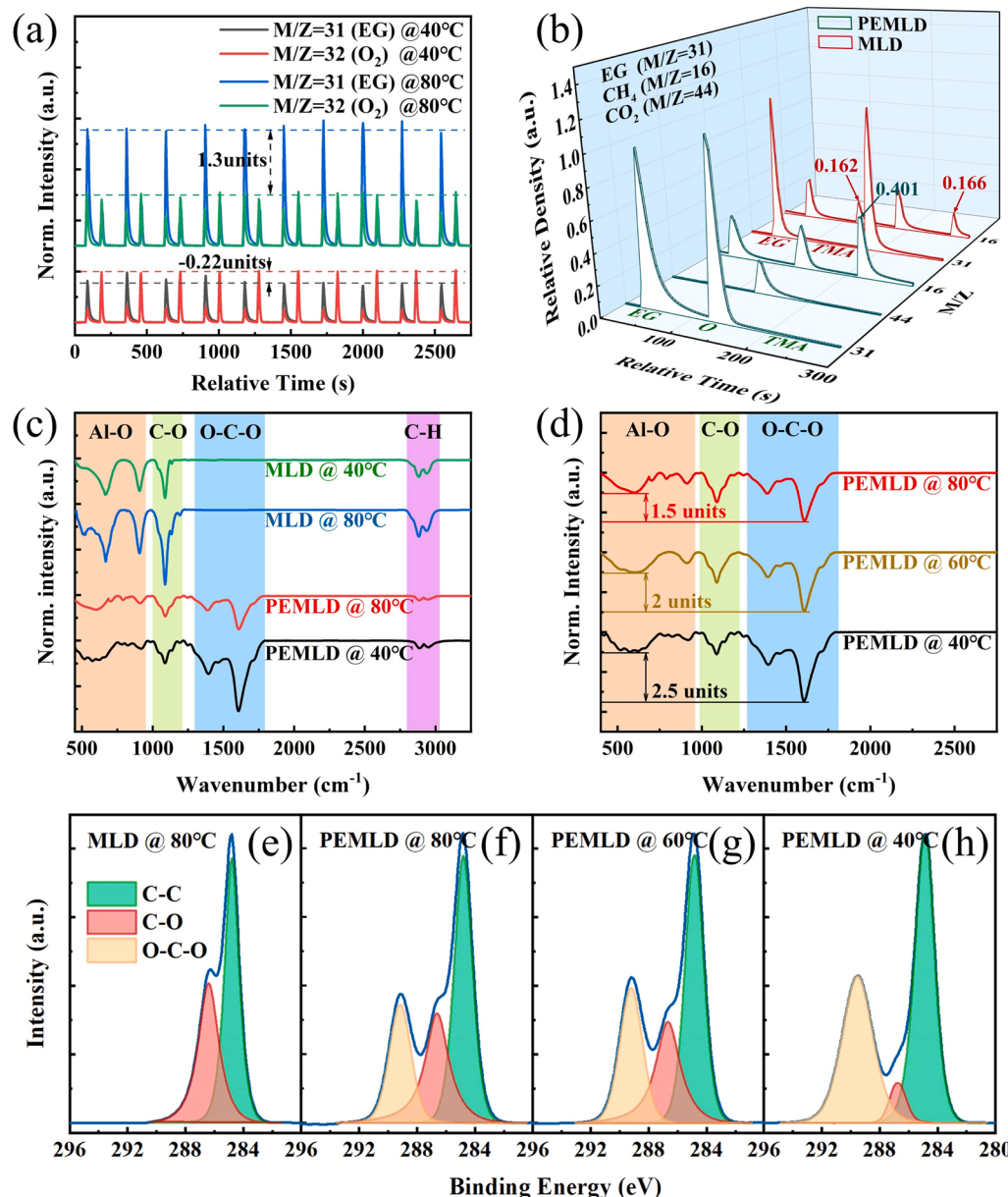
re-engaged in the oxidation reaction with O plasma (reaction (3)). This ABC-type reaction sequence occurring sequentially from EG, O plasma, and TMA can be called PEMLD. Eq. (3) describes the surface half-reaction between -CH<sub>3</sub>\* and O plasma, with the chemical bonds exposed on the substrate surface, are marked with a “\*” [25].



The evolutions of EG (M/Z = 31) and O<sub>2</sub> (M/Z = 16) molecules during PEMLD at different temperatures were monitored by *in-situ* quadrupole mass spectrometry (QMS). As shown in Fig. 2a, the partial pressure of EG molecules in the reaction chamber under 40 °C was significantly lower than that under 80 °C due to the severe condensation, as well as the grievous physisorption that generated abundant unreacted active site -CH<sub>3</sub> on the substrate. Furthermore, the comparison of the evolution of CH<sub>4</sub> and CO<sub>2</sub> by-products in the MLD and PEMLD at 40 °C revealed the injection of O plasma in PEMLD accompanied by the generation of abundant CH<sub>4</sub> and CO<sub>2</sub> by-products (Eq. (3), Fig. 2b). The O plasma did not only react with the residual -CH<sub>3</sub> caused by the transient steric hindrance, but also smoothly diffused into the "forbidden zone" under the structural steric hindrance due to its small spatial volume to establish contact with -CH<sub>3</sub>. After subsequent TMA pulses, more generated CH<sub>4</sub> by-products than using MLD forced more -OH into surface reaction, contributing to O plasma. Consequently, the full infiltration of O plasma promoted the saturation of surface reaction, allowing

PEMLD to proceed stably at 40 °C (Fig. 1b).

Fourier-transform infrared spectroscopy (FTIR) was used for the chemical composition after the assistance of O plasma. As shown in Fig. 2c, a decrease in FTIR intensity of the bending and stretching vibration bands of C—H bonds (2780–3000 cm<sup>-1</sup>) [26] was noticed, which represented the consumption of the surface unreacted active site -CH<sub>3</sub> by O plasma. Also, the more random orientation of the bending and stretching vibration bands of Al—O bonds was induced between 490 and 950 cm<sup>-1</sup>, suggesting amorphous composition similar to that Al<sub>2</sub>O<sub>3</sub> grown by ALD [27,28]. Meanwhile, bending and stretching vibration bands of O—C—O bonds were recorded at wavelengths of 1300–1780 cm<sup>-1</sup> [29,30]. This characteristic has never been observed for alucone grown by MLD, demonstrating the capability of O plasma in oxidizing C-H to C-OH as confirmed by the opposite trends of the bending and stretching vibration bands of C-O (1000–1200 cm<sup>-1</sup>) [31] and O-C-O. The occurrence of this hydroxylation reaction did not only solve the issue of double reaction (unique to homobifunctional precursors) by creating active sites -OH through the oxidation of H on the C backbone, but also crosslinked otherwise parallel and independent C-C backbone. Besides, more O-C-O composition was observed at lower process temperatures (Fig. 2d), owing to the severe steric hindrance which provided sufficient reaction paths for film crosslinking. Simultaneously, the comparison of the evolution of CH<sub>4</sub> (M/Z = 16) by-products and CO<sub>2</sub> (M/Z = 44) by-products during PEMLD at 40 °C



and 80 °C was performed by normalizing the O<sub>2</sub> (M/Z = 32) partial pressure as the reference. As can be seen in Fig. 3a, the chemical reaction proportion of EG was less at 40 °C compared to 80 °C due to a more severe condensation and confirmed by the presence of fewer CH<sub>4</sub> by-products after EG injection. By contrast, more unreacted active sites -CH<sub>3</sub> re-exposed to the substrate surface at 40 °C due to the desorption of EG molecules could provide conditions for the reaction with O plasma, and more O plasma surface chemical reactions led to larger CO<sub>2</sub> by-product partial pressure. Thus, films grown by PEMLD were referred to as PEMLD-AlCO in subsequent studies. Analogously, MLD-Alucone and PEALD-Al<sub>2</sub>O<sub>3</sub> were used for ease of comparison.

X-ray photoelectron spectroscopy (XPS) was employed to compare the compositions and structures of PEMLD-AlCO and MLD-Alucone grown at 40 °C. The elements C, O, and Al were observed as the only constituent elements in both compounds. The elemental ratio of MLD-Alucone film was determined from the XPS survey spectrum as C:O:Al = 1:0.58:0.22 (Fig. S2), reasonable for a typical structure. By comparison, the elemental ratio of PEMLD-AlCO film was determined as C:O:Al = 1:1.45:0.47 (Fig. S3). The increase in the elemental content of Al

and O elucidated an elevated proportion of inorganic components. The C 1s peak of PEMLD-AlCO can be deconvoluted into three different bond configurations with C—C, C—O, and O—C—O at 284.8 eV, 286.6 eV, and 289.2 eV, respectively.[32,33] The characteristic peak of O—C—O bonds was unique to PEMLD-AlCO and represented the cross-linking component (Fig. 2e–f). More O—C—O bond configurations were also generated under lower temperatures, including O—C—O:C—O = 0.82:1 at 80 °C, 1.05:1 at 60 °C, and 7.50:1 at 40 °C (Table 1). Thus, the decrease in temperature was accompanied by more conversion of the C—O bond configurations into O—C—O bond configurations (Fig. 2f–h), consistent with the FTIR analysis data.

Overall, O plasma was capable of oxidizing the unreacted active site (-CH<sub>3</sub>) caused by steric hindrance, as well as creating active sites through the oxidation of H on the C backbone. The surface chemical reaction model of PEMLD is described in Fig. 3(b–d). (b) After the EG injection, more unreacted active sites -CH<sub>3</sub> remained on the surface due to the self-limiting steric hindrance effect. Moreover, the double reaction of EG caused the formation of some surface termination sites. (c) The subsequently injected O plasma was capable of oxidizing the

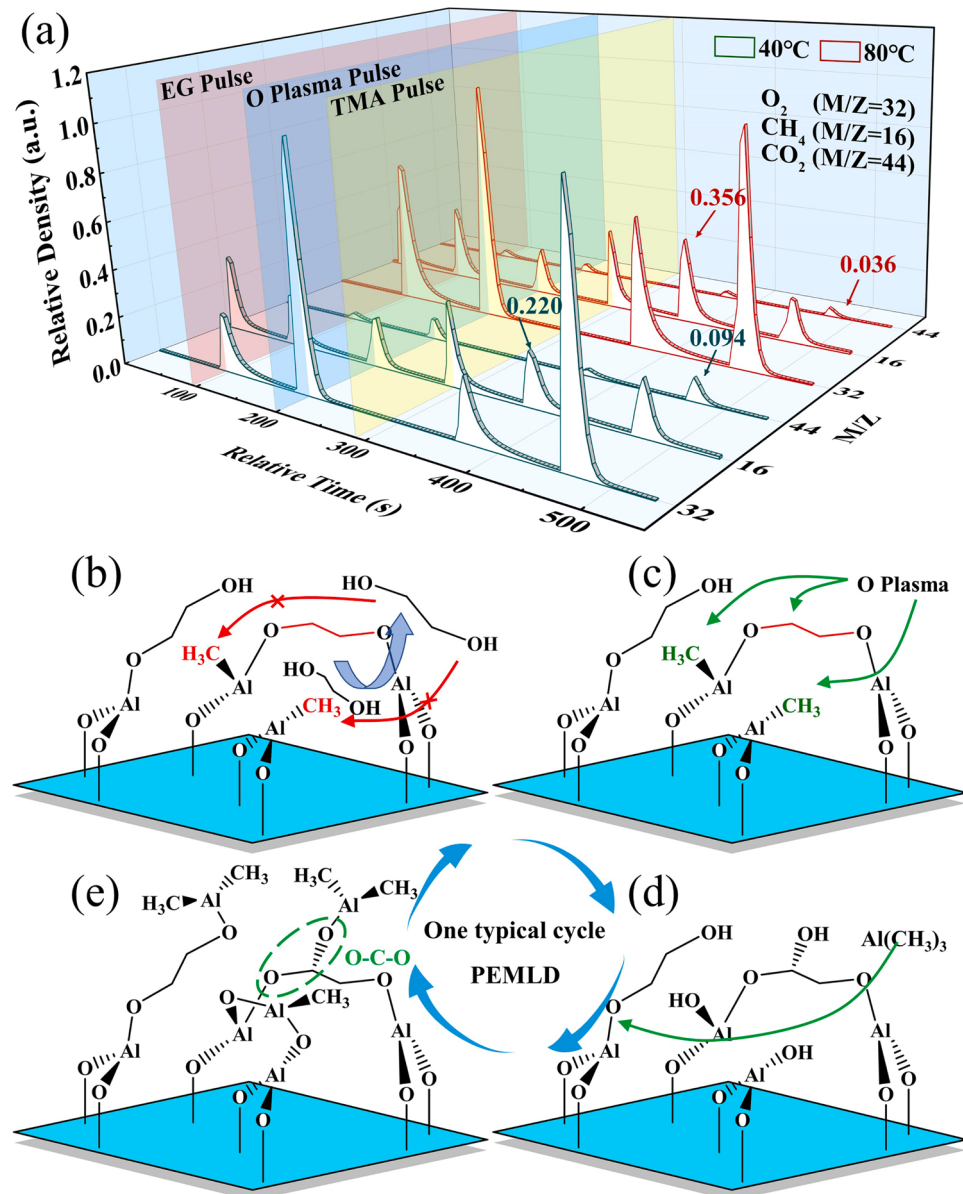


**Fig. 3.** (a) *In-situ* QMS results during PEMLD at 40 °C and 80 °C. Schematic diagram of surface chemical reaction in one typical cycle: (b) The reaction barriers induced by steric hindrance and double reaction from EG. (c) Oxidation by O plasma. (d) Pulse of TMA. (e) Formation of hybridization and crosslinking.

**Table 1**

The proportions of different bond configurations with C-C, C-O, and O-C-O obtained from XPS high-resolution spectra of C 1s.

	C-C	C-O	O-C-O	O-C-O/C-O
MLD-Alucone @ 80 °C	1	0.76	0	0
PEMLD-AlCO @ 80 °C, 5 s plasma pulse	1	0.62	0.51	0.82:1
PEMLD-AlCO @ 60 °C, 5 s plasma pulse	1	0.56	0.59	1.05:1
PEMLD-AlCO @ 40 °C, 5 s plasma pulse	1	0.10	0.75	7.50:1
PEMLD-AlCO @ 40 °C, 3 s plasma pulse	1	0.46	0.69	1.50:1
PEMLD-AlCO @ 40 °C, 1 s plasma pulse	1	0.77	0.55	0.71:1

residual -CH<sub>3</sub> and H on the C backbone to produce -OH, which can react with TMA. (d) TMA was injected and reacted with -OH to form Al—O bonds. (e) AlCO film was formed.

Similarly, the oxidation of O plasma also occurred through a self-saturating surface reaction related to the effective partial pressure time in the reaction chamber. Accordingly, the plasma pulse times of 1, 3, 5, 7, 9 and 11 s were tested to gain better insights, and Al—O

characteristic peak was used as the reference intensity. As presented in Fig. 4a, the relative content of O—C—O bonds gradually increased with the extension of O plasma pulse time, while the content of the C—O bond declined, implying a self-saturating conversion between the two configurations. The two self-consistent trend curves revealed 5 s pulse time of O plasma sufficient to achieve a saturated surface reaction. The C environments of the PEMLD-AlCO at different O plasma pulse times were further analyzed by XPS. In Fig. 4b-d, the O plasma pulse time increased, and more conversion of C—O bond configurations to O—C—O bond configurations occurred. The XPS high-resolution spectra of C 1s revealed the presence of O-C-O:C-O = 0.71:1 at a pulse of 1 s, 1.50:1 at a pulse of 3 s, and 7.50:1 at a pulse of 5 s (Table 1). Also, extending the O plasma pulse time can effectively increase the proportion of inorganic components in PEMLD-AlCO, as shown by scanning electron microscopy and energy-dispersive X-ray spectroscopy (SEM-EDS, Fig. S4).

Based on the growth mechanism and film composition of PEMLD, the next step was to calculate the growth rate per cycle (GPC), mass gain per cycle (MGPC), and density of the relevant film processes. To this end,

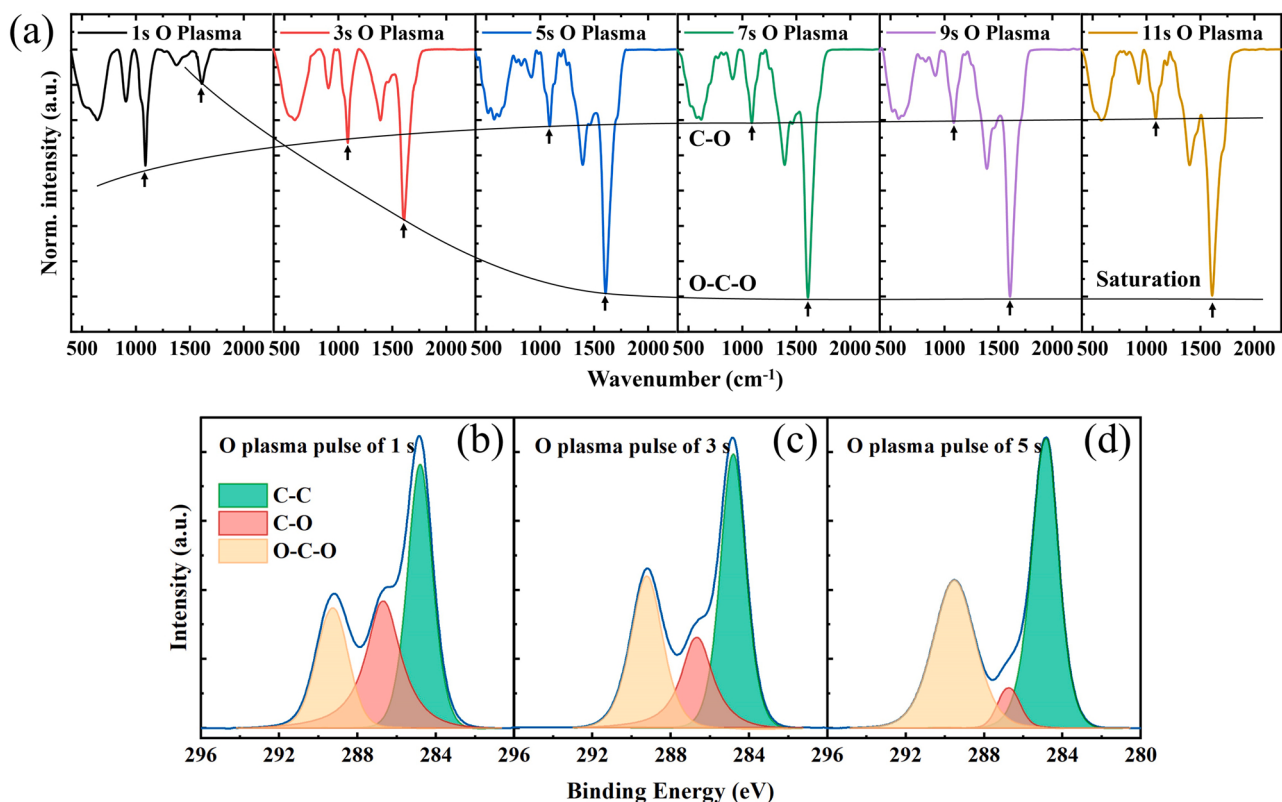


**Fig. 4.** The self-saturating surface reaction of O plasma. (a) FTIR and (b-d) XPS high-resolution spectra (C 1s) of the barrier films grown by PEMLD at various O plasma pulse times.

QCM and ellipsometry tests were used and the data are summarized in Table 2 together with the refractive index values. The EG molecules exhibited severe surface condensation at 40 °C due to the generation of physisorption. The physisorbed EG molecules failed to detach from the substrate surface during the purge process, inducing large numbers of surface CVD reactions and resulting in larger GPC and MGPC amounts when compared to those obtained 80 °C [34]. The less produced GPC during PEMLD at 40 °C demonstrated that O plasma could effectively promote the desorption of EG molecules with surface reaction regaining its self-limiting nature. A similar result was also obtained at the temperature of 80 °C. Additionally, the new active sites (-OH) introduced by O plasma enabled more TMA molecules to participate in the surface cross-linking reaction, leading to higher MGPC and density. For further performance comparison, Al<sub>2</sub>O<sub>3</sub> film was prepared by PEALD at 40 °C. As depicted in Fig. S5, the density of films grown by PEMLD looked close to that of PEALD-Al<sub>2</sub>O<sub>3</sub>. Also, a similar trend was reflected in the refractive index. The transmission in visible wavelength and surface

morphology are given in Fig. S6 and Fig. S7.

### 3.3. Barrier performance and flexibility

Moisture barrier performance and flexibility are vital features of flexible encapsulation. Hence, the WVTR values of 50 nm-PEMLD-AlCO, 50 nm-MLD-alucone, and 50 nm-PEALD-Al<sub>2</sub>O<sub>3</sub> grown at 40 °C were measured via electrical calcium testing (Fig. 5a).

As shown in the inset of Fig. 5a, MLD-alucone exhibited an inferior moisture barrier performance with a WVTR value of  $3.78 \times 10^{-3} \text{ g m}^{-2} \text{ day}^{-1}$  (Linear area), thereby ineffective for the protection of electronics. Meanwhile, the unstable nature of MLD-alucone facilitated its rapid degradation after 250 min of exposure to the atmospheric environment (Degraded area). By contrast, PEMLD-AlCO with a WVTR value of  $1.44 \times 10^{-5} \text{ g m}^{-2} \text{ day}^{-1}$  demonstrated a comparable moisture barrier performance to PEALD-Al<sub>2</sub>O<sub>3</sub> with a WVTR of  $1.17 \times 10^{-5} \text{ g m}^{-2} \text{ day}^{-1}$ . Besides, no significant damage was observed over one month owing to the densification and cross-linking by O plasma.

After 10,000 bends with a 3 mm bending radius, the WVTR value of PEALD-Al<sub>2</sub>O<sub>3</sub> increased by more than two orders of magnitude (Fig. 5b), suggesting complete damage to the barrier after the intense mechanical motion. Inversely, the WVTR value of PEMLD-AlCO showed only some enhancement from  $1.44 \times 10^{-5} \text{ g m}^{-2} \text{ day}^{-1}$  to  $1.50 \times 10^{-5} \text{ g m}^{-2} \text{ day}^{-1}$  (Fig. 5b). The uniformly distributed carbon backbone inside the film contributed to the excellent flexibility. In Fig. 5c, the grayscale images of calcium during corrosion exhibited the moisture corrosion paths after bending, where striate corrosion in PEALD-Al<sub>2</sub>O<sub>3</sub> films elucidated cracking in the direction perpendicular to bending. However, the complete failure of moisture barrier performance of MLD-alucone after bending prevented calcium testing. Additionally, the optical microscopy images illustrated damage to PEMLD-AlCO, PEALD-Al<sub>2</sub>O<sub>3</sub>, MLD-alucone grown at 40 °C, and MLD-alucone grown at 80 °C (Fig. 5d). Note that MLD-alucone grown at 80 °C was utilized as a

**Table 2**

Summary of GPC, MGPC, density, and refractive index of barrier films grown by various processes.

	GPC [nm/ cycle]	MGPC [ng/ cm <sup>2</sup> /cycle]	Density [g/ cm <sup>3</sup> ]	Refractive index
PEMLD-AlCO @ 40 °C	0.361	92.6	2.565	1.61
PEMLD-AlCO @ 80 °C	0.356	84.2	2.365	1.57
MLD-alucone @ 80 °C	0.384	82.0	2.14	1.54
MLD-alucone @ 40 °C	0.470	91.9	1.96	1.49
PEALD-Al <sub>2</sub> O <sub>3</sub> @ 40 °C	0.163	42.7	2.620	1.62

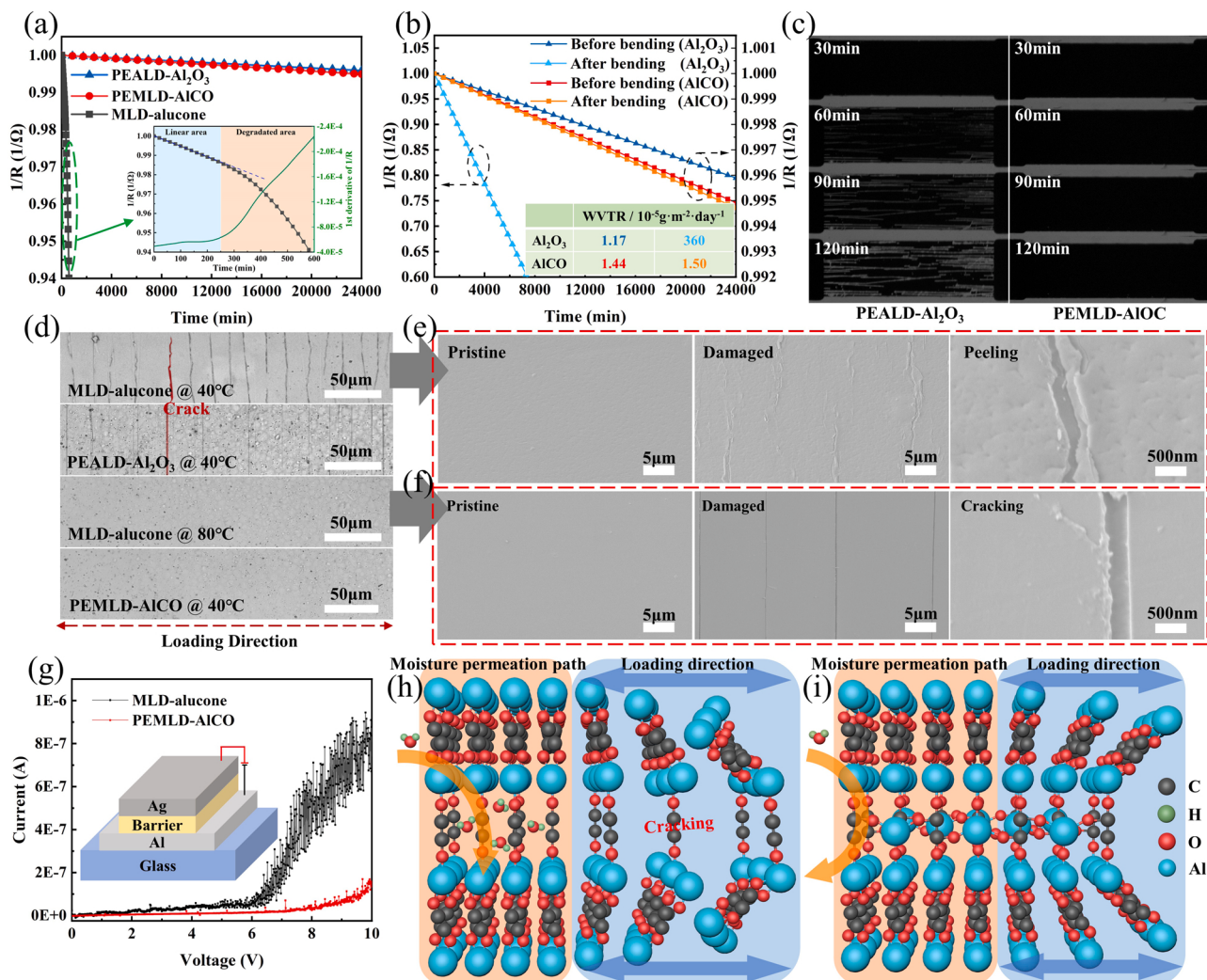


**Fig. 5.** Comparison of moisture barrier performance by electrical calcium test: (a) WVTR of PEALD- $\text{Al}_2\text{O}_3$ , PEMLD-AlCO and MLD-alucone under the same thickness from  $1/R$ -Time curve. (b) WVTR of PEALD- $\text{Al}_2\text{O}_3$  and PEMLD-AlCO before and after 10,000 bends with a 3 mm bending radius from  $1/R$ -Time curve. Crack evolution behavior of barrier films after 10,000 bends with a 3 mm bending radius: (c) Grayscale images of calcium encapsulated by PEALD- $\text{Al}_2\text{O}_3$  and PEMLD-AlCO during corrosion from optical calcium corrosion testing. (d) Optical microscope images of barrier films grown by various processes. Microscopic crack mechanism of MLD-alucone grown at (e) 40 °C and (f) 80 °C from SEM images. (g) Leakage current of barrier layers as a function of voltage. Structure schematic diagram of (h) MLD-alucone and (i) PEMLD-AlCO account for the theoretical explanation of flexibility and barrier performance.

superior film for comparison. The MLD-alucone grown at 40 °C exhibited inferior flexibility when compared to the superior one induced by failed toughness due to the increase of defects inside the films. Additionally, the loss in toughness induced more convoluted and unstructured cracks. Therefore, superior-alucone cracks were made at a bending radius of 1 mm, and the microscopic crack mechanism was studied by SEM imaging. As shown in Fig. 5ef, a peeling behavior was noticed in MLD-alucone grown at 40 °C, corroborating an inferior toughness. Moreover, the crack behavior of PEMLD-AlCO also occurred at a bending radius of 1 mm. Unlike MLD-alucone grown at 40 °C, the crosslinking caused by the oxidation of H on the C backbone by O plasma resulted in a substantially increased toughness (Fig. S8), conducive to the excellent flexibility.

Overall, the film densification and crosslinking brought by O plasma could effectively enhance the moisture barrier performance and toughness. A theoretical explanation is provided in Fig. 5h-i, where the middle and both sides of the model represent the microscopic and macroscopic structures in alucone and AlCO, respectively. The unsaturated adsorption on the surface caused by steric hindrance during MLD at 40 °C generated substantial defects inside the film, providing paths for moisture penetration. Furthermore, the formation of cracking under

complex mechanical motions by the defects combined with as weaker interaction forces between C-C backbone generated inferior mechanical properties (Fig. 5h). Besides, the filling and creation of active sites during O plasma blocked the moisture permeation paths created by defects, facilitating crosslinking between the otherwise parallel and independent C-C backbones (Fig. 5i). The enhanced interaction force between C-C backbones prevented the occurrence of cracking under complex mechanical motions, resulting in excellent moisture barrier performance and flexibility. Moreover, leakage current testing demonstrated that PEMLD-AlCO have only a few defects in comparison with the MLD-alucone of the same thickness (Fig. 5g).

### 3.4. Application of encapsulation in flexible perovskite solar cells

Both top and bottom encapsulation in F-PSCs would be indispensable for moisture permeability through PEN substrate. Hence, PEMLD-AlCO was placed below PEN and above the device for the bottom and top encapsulation, respectively (Fig. 6a).

$\text{Al}_2\text{O}_3$ , alucone, and AlCO grown by respectively PEALD, MLD, and PEMLD were adopted as barrier layers for  $\text{FA}_x\text{MA}_{1-x}\text{PbI}_3$  films to investigate the mildness of the process. As shown in Fig. S9,

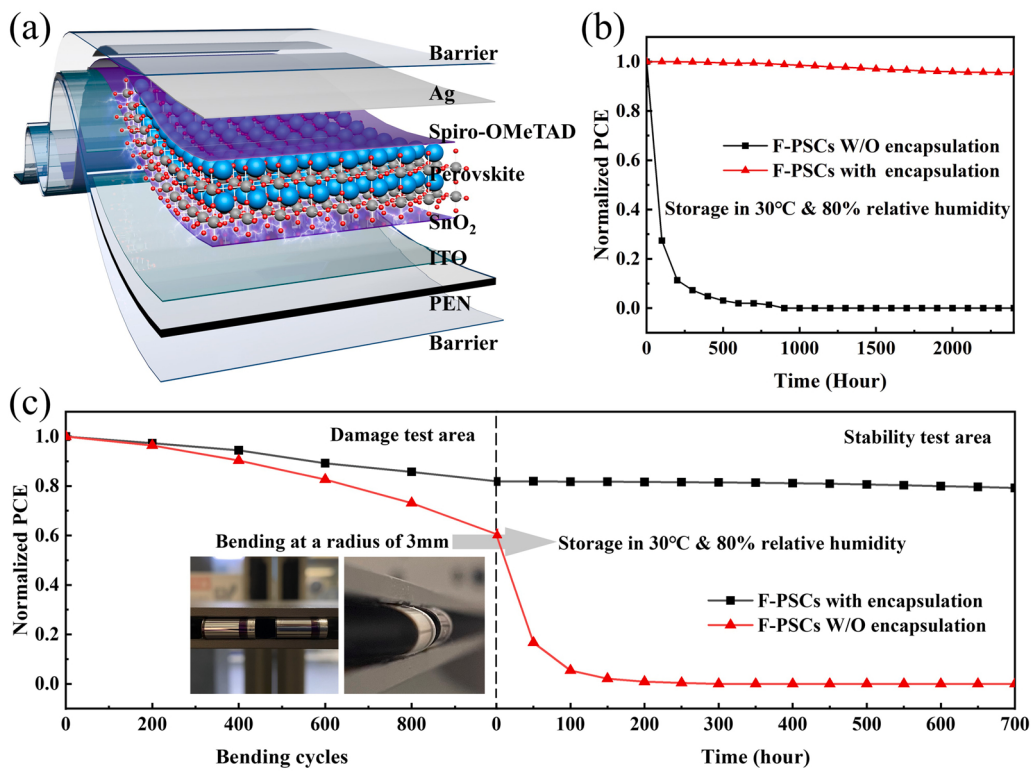
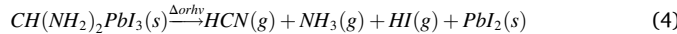


**Fig. 6.** (a) Structure schematic diagram of the encapsulated perovskite solar cells. Time evolution of normalized PCE for the F-PSCs with and without encapsulation under 30 °C and 80 % relative humidity (b) before bending, (c) during and after bending.

$\text{FA}_x\text{MA}_{1-x}\text{PbI}_3$  underwent severe decomposition due to the O plasma treatment during PEALD (Eq. (4)) [35], corroborated by the increase in the relative content of  $\text{PbI}_2$  after encapsulation.



Inversely, the damage from O plasma was minimized in PEMLD, resulting in a mild encapsulation process similar to MLD. Thus, EG effectively blocked and absorbed O plasma during PEMLD to avoid its penetration into  $\text{FA}_x\text{MA}_{1-x}\text{PbI}_3$  film. Additionally, F-PSCs were encapsulated by PEMLD at 80 °C and 40 °C to verify the damage caused by the process temperature. As presented in Fig. S10a, the severely damaged F-PSCs only preserved 32.7 % of their initial PCE after encapsulation at 80 °C. Only 0.13 % of efficiency was lost after encapsulation by PEMLD at 40 °C, as shown by the I-V curves in Fig. S10b. The distribution of the initial PCE for 16 cells confirmed the excellent uniformity of the encapsulation process (Fig. S10c-d). A comparison of F-PSCs with and without encapsulation placed at 30 °C and 80 % relative humidity revealed severe corrosion of F-PSCs without encapsulation after 72 h, while the F-PSCs with encapsulation remained intact. The corresponding changes in efficiency are shown in Fig. 6b. The encapsulated F-PSCs were still shown intact with 95 % of the initial efficiency maintained after 2400 h. Moreover, in order to investigate the performance degradation of F-PSCs with and without encapsulation after bending, the F-PSCs with and without encapsulation were bent 1000 times at a bending radius of 3 mm for damage testing, and subsequently, stored at 30 °C & 80 % relative humidity for 720 h. The damage test lasts 4000 s, as depicted in the "Damage test area" of Fig. 6c, the PCE degradation of F-PSCs without encapsulation is more severe than that of F-PSCs with encapsulation due to accelerated moisture penetration during the bending process. The F-PSCs without encapsulation completely failed after 300 h, while the F-PSCs with encapsulation preserved 96.8 % of its initial PCE after 720 h, as depicted by the PCE curve in the "Stability test area".

#### 4. Conclusions

The challenges of steric hindrance in MLD were analyzed at 40 °C, considered a mild temperature for F-PSCs encapsulation. A novel ABC-type PEMLD technology with sequential pulses of EG, O plasma, and TMA was proposed by taking advantage of the small spatial volume and high activity of O plasma. As consequence, an AlCO film with excellent barrier performance and flexibility was successfully prepared as a moisture barrier for F-PSCs encapsulation. The results showed that O plasma was capable of oxidizing the unreacted active sites (-CH<sub>3</sub>) caused by a steric hindrance to forming densified films. The O plasma can also create active sites through the oxidation of H on C backbone, cross-linking otherwise parallel and independent C-C backbone. The AlCO film exhibited excellent barrier performance with a WVTR of  $1.44 \times 10^{-5} \text{ g m}^{-2} \text{ day}^{-1}$ , while its potent crack-inhibition ensured a 95 % initial barrier performance after 10,000 bends with a 3 mm bending radius. The F-PSCs encapsulated with a 50 nm-AlCO maintained 95 % of their initial efficiency after 2400 h when placed at 30 °C and 80 % relative humidity. To the best of our knowledge, this is the first report dealing with O plasma-induced crosslinking in MLD technology, and the proposed reaction mechanism would be useful for the modification of organic and organic-inorganic hybrid films grown by MLD.

#### CRediT authorship contribution statement

**Zhenyu Wang:** Conceptualization, Methodology, Validation, Writing – original draft. **Jintao Wang:** Methodology, Validation. **Ze Li:** Validation. **Ziqiang Chen:** Data curation. **Lianchao Shangguan:** Validation. **Siyu Fan:** Investigation. **Yu Duan:** Supervision, Writing – review & editing.

## Declaration of Competing Interest

The authors declare that they have no known competing financial interests or personal relationships that could have appeared to influence the work reported in this paper.

## Data Availability

Data will be made available on request.

## Acknowledgments

The authors thank support from the National Natural Science Foundation of China (Grant nos. 61974054 and 61675088), the International Science & Technology Cooperation Program of Jilin (Grant no. 20190701023GH), the Scientific and Technological Developing Scheme of Jilin Province (Grants no. 20200401045GX), and the Project of Science and Technology Development Plan of Jilin Province (Grant no. 20190302011G).

## Appendix A. Supporting information

Supplementary data associated with this article can be found in the online version at [doi:10.1016/j.nanoen.2023.108232](https://doi.org/10.1016/j.nanoen.2023.108232).

## References

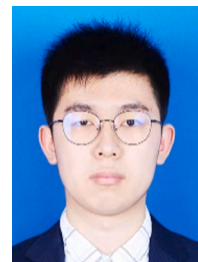
- [1] S.I. Seok, M. Gratzel, N.-G. Park, Methodologies toward highly efficient perovskite solar cells, *Small* 14 (2018), <https://doi.org/10.1002/smll.201704177>.
- [2] M.A. Green, A. Ho-Baillie, H.J. Snaith, The emergence of perovskite solar cells, *Nat. Photonics* 8 (2014) 506–514, <https://doi.org/10.1038/nphoton.2014.134>.
- [3] N.R.E. Laboratory, Cell Efficiency Chart. (<https://www.nrel.gov/pv/cell-efficiency.html>).
- [4] J. Ramanujam, D.M. Bishop, T.K. Todorov, O. Gunawan, J. Rath, R. Nekovei, E. Artegiani, A. Romeo, Flexible CIGS, CdTe and a-Si:H based thin film solar cells: a review, *Prog. Mater. Sci.* 110 (2020) 20, <https://doi.org/10.1016/j.pmatsci.2019.100619>.
- [5] S. Albrecht, B. Rech, On top of commercial photovoltaics, *Nat. Energy* 2 (2017), <https://doi.org/10.1038/nenergy.2016.196>.
- [6] Q. Wali, F.J. Iftikhar, M.E. Khan, A. Ullah, Y. Iqbal, R. Jose, Advances in stability of perovskite solar cells, *Org. Electron.* 78 (2020) 17, <https://doi.org/10.1016/j.orgel.2019.105590>.
- [7] L. Meng, J. You, Y. Yang, Addressing the stability issue of perovskite solar cells for commercial applications, *Nat. Commun.* 9 (2018), <https://doi.org/10.1038/s41467-018-07255-1>.
- [8] C.C. Boyd, R. Checharoen, T. Leijtens, M.D. McGehee, Understanding degradation mechanisms and improving stability of perovskite photovoltaics, *Chem. Rev.* 119 (2019) 3418–3451, <https://doi.org/10.1021/acs.chemrev.8b00336>.
- [9] R. Wang, M. Mujahid, Y. Duan, Z.-K. Wang, J. Xue, Y. Yang, A review of perovskites solar cell stability, *Adv. Funct. Mater.* 29 (2019), <https://doi.org/10.1002/adfm.201808843>.
- [10] J.-H. Woo, S.-Y. Park, D. Koo, M.H. Song, H. Park, J.-Y. Kim, Highly elastic and corrosion-resistant metallic glass thin films for flexible encapsulation, *Acs Appl. Mater. Interfaces* 14 (2022) 5578–5585, <https://doi.org/10.1021/acsami.1c20551>.
- [11] L.J. Sutherland, H.C. Weerasinghe, G.P. Simon, A review on emerging barrier materials and encapsulation strategies for flexible perovskite and organic photovoltaics, *Adv. Energy Mater.* 11 (2021), <https://doi.org/10.1002/aenm.202101383>.
- [12] J.S. Park, H. Chae, H.K. Chung, S.I. Lee, Thin film encapsulation for flexible AM-OLED: a review, *Semicond. Sci. Technol.* 26 (2011) 8, <https://doi.org/10.1088/0268-1242/26/3/034001>.
- [13] D. Yu, Y.-Q. Yang, Z. Chen, Y. Tao, Y.-F. Liu, Recent progress on thin-film encapsulation technologies for organic electronic devices, *Opt. Commun.* 362 (2016) 43–49, <https://doi.org/10.1016/j.optcom.2015.08.021>.
- [14] E.G. Jeong, J.H. Kwon, K.S. Kang, S.Y. Jeong, K.C. Choi, A review of highly reliable flexible encapsulation technologies towards rollable and foldable OLEDs, *J. Inf. Disp.* 21 (2020) 19–32, <https://doi.org/10.1080/15980316.2019.1688694>.
- [15] Y.I. Lee, N.J. Jeon, B.J. Kim, H. Shim, T.Y. Yang, S.I. Seok, J. Seo, S.G. Im, A low-temperature thin-film encapsulation for enhanced stability of a highly efficient perovskite solar cell, *Adv. Energy Mater.* 8 (2018), 1701928.
- [16] H. Wang, Y. Zhao, Z. Wang, Y. Liu, Z. Zhao, G. Xu, T.-H. Han, J.-W. Lee, C. Chen, D. Bao, Y. Huang, Y. Duan, Y. Yang, Hermetic seal for perovskite solar cells: an improved plasma enhanced atomic layer deposition encapsulation, *Nano Energy* 69 (2020), <https://doi.org/10.1016/j.nanoen.2019.104375>.
- [17] C.-Y. Chang, K.-T. Lee, W.-K. Huang, H.-Y. Siao, Y.-C. Chang, High-performance, air-stable, low-temperature processed semitransparent perovskite solar cells enabled by atomic layer deposition, *Chem. Mater.* 27 (2015) 5122–5130, <https://doi.org/10.1021/acs.chemmater.5b01933>.
- [18] Y. Li, Y. Xiong, W. Cao, Q. Zhu, Y. Lin, Y. Zhang, M. Liu, F. Yang, K. Cao, R. Chen, Flexible PDMS/Al2O3 nanolaminates for the encapsulation of blue OLEDs, *Adv. Mater. Interfaces* 8 (2021), <https://doi.org/10.1002/admi.202100872>.
- [19] J.-H. Han, T.-Y. Kim, D.-Y. Kim, H.L. Yang, J.-S. Park, Water vapor and hydrogen gas diffusion barrier characteristics of Al2O3-alucone multi-layer structures for flexible OLED display applications, *Dalton Trans.* 50 (2021) 15841–15848, <https://doi.org/10.1039/d1dt02989d>.
- [20] H. Wang, Z. Wang, X. Xu, W. Zhao, D. Wu, M. Muhammad, Y. Liu, C. Chen, B. Liu, Y. Duan, A. Novel, Nucleation inducer for ultrathin au anodes in high efficiency and flexible organic optoelectronic devices, *Adv. Opt. Mater.* 8 (2020), <https://doi.org/10.1002/adom.201901320>.
- [21] H. Wang, Z. Wang, X. Xu, Y. Liu, C. Chen, P. Chen, W. Hu, Y. Duan, Multiple short pulse process for low-temperature atomic layer deposition and its transient steric hindrance, *Appl. Phys. Lett.* 114 (2019), <https://doi.org/10.1063/1.5095515>.
- [22] A.A. Dameron, D. Seghete, B.B. Burton, S.D. Davidson, A.S. Cavanagh, J. A. Bertrand, S.M. George, Molecular layer deposition of alucone polymer films using trimethylaluminum and ethylene glycol, *Chem. Mater.* 20 (2008) 3315–3326, <https://doi.org/10.1021/cm703297t>.
- [23] T. Muneshwar, K. Cadien, Surface reaction kinetics in atomic layer deposition: an analytical model and experiments, *J. Appl. Phys.* 124 (2018), <https://doi.org/10.1063/1.5044456>.
- [24] S.M. George, B. Yoon, A.A. Dameron, Surface chemistry for molecular layer deposition of organic and hybrid organic–inorganic polymers, *Acc. Chem. Res.* 42 (2009) 498–508, <https://doi.org/10.1021/ar800105q>.
- [25] H. Wang, Y. Liu, H. Liu, Z. Chen, P. Xiong, X. Xu, F. Chen, K. Li, Y. Duan, Effect of various oxidants on reaction mechanisms, self-limiting natures and structural characteristics of Al2O3 films grown by atomic layer deposition, *Adv. Mater. Interfaces* 5 (2018), <https://doi.org/10.1002/admi.201701248>.
- [26] Y.-S. Park, H. Kim, B. Cho, C. Lee, S.-E. Choi, M.M. Sung, J.S. Lee, Intramolecular and intermolecular interactions in hybrid organic-inorganic alucone films grown by molecular layer deposition, *Acs Appl. Mater. Interfaces* 8 (2016) 17489–17498, <https://doi.org/10.1021/acsmami.6b01856>.
- [27] B.H. Lee, B. Yoon, V.R. Anderson, S.M. George, Alucone alloys with tunable properties using alucone molecular layer deposition and Al2O3 atomic layer deposition, *J. Phys. Chem. C* 116 (2012) 3250–3257, <https://doi.org/10.1021/jp209003h>.
- [28] N. Batra, J. Gope, J. Panigrahi Vandana, R. Singh, P.K. Singh, Influence of deposition temperature of thermal ALD deposited Al2O3 films on silicon surface passivation, *Aip Adv.* 5 (2015), <https://doi.org/10.1063/1.4922267>.
- [29] S. Sahoo, C. Chakraborti, P. Behera, S. Mishra, FTIR and Raman spectroscopic investigations of a norfloxacin/Carbopol934 polymeric suspension, *J. Young Pharm.: JYP* 4 (2012) 138–145, <https://doi.org/10.4103/0975-1483.100017>.
- [30] J. Kwon, M. Dai, M.D. Halls, Y.J. Chabal, Detection of a formate surface intermediate in the atomic layer deposition of high-k dielectrics using ozone, *Chem. Mater.* 20 (2008) 3248–3250, <https://doi.org/10.1021/cm703667h>.
- [31] D.N. Goldstein, J.A. McCormick, S.M. George, Al2O3 atomic layer deposition with trimethylaluminum and ozone studied by in situ transmission FTIR spectroscopy and quadrupole mass spectrometry, *J. Phys. Chem. C* 112 (2008) 19530–19539, <https://doi.org/10.1021/jp804296a>.
- [32] A. Jejurikar, X.T. Seow, G. Lawrie, D. Martin, A. Jayakrishnan, L. Grondahl, Degradable alginate hydrogels crosslinked by the macromolecular crosslinker alginic dialdehyde, *J. Mater. Chem.* 22 (2012) 9751–9758, <https://doi.org/10.1039/c2jm30564j>.
- [33] M.M.H. Asif, A. Qaiser, X-ray photoelectron spectroscopy characterization of polyaniline-cellulose ester composite membranes, *Mater. Sci. Forum* 657 (2010) 35–45, <https://doi.org/10.4028/www.scientific.net/MSF.657.35>.
- [34] X. Liang, M. Yu, J. Li, Y.-B. Jiang, A.W. Weimer, Ultra-thin microporous-mesoporous metal oxide films prepared by molecular layer deposition (MLD), *Chem. Commun.* (2009) 7140–7142, <https://doi.org/10.1039/b91188h>.
- [35] L. Ma, D. Guo, M. Li, C. Wang, Z. Zhou, X. Zhao, F. Zhang, Z. Ao, Z. Nie, Temperature-dependent thermal decomposition pathway of organic-inorganic halide perovskite materials, *Chem. Mater.* 31 (2019) 8515–8522, <https://doi.org/10.1021/acs.chemmater.9b03190>.

**Zhenyu Wang** is a doctor candidate of Jilin University, China. He received the B.S. degree from the College of Electronic Science & Engineering, Jilin University, China in 2018. His research focuses on the atomic layer deposition and thin film encapsulation for organic photoelectric devices.





**Jintao Wang** is a doctor candidate of Jilin University, China. He received his B.S. degree from the School of Physics, Changchun University of Science and Technology. His research interests include perovskite solar cells and perovskite light-emitting diodes.



**Lianchao Shangguan** is a master candidate of Jilin University, China. He received the B.S. degree from the College of Electronic Science & Engineering, Jilin University, China in 2020. His research focuses on the thin film encapsulation of optoelectronic devices by chemical vapor deposition technology.



**Ze Li** received his master degree from the College of Electronic Science & Engineering, Jilin University, China in 2022. His research focuses on the design of flexible encapsulation film with low residual stress.



**Siyu Fan** is a master candidate of Jilin University, China. He received the B.S. degree from the College of Electrical Engineering and Its Automation, Changchun University of Science and Technology in 2021. His research focuses on the atomic layer deposition and the development of novel organic light-emitting diodes.



**Ziqiang Chen** is a master candidate of Jilin University, China. He received his B.S. degree from the School of Electrical Engineering, Anhui Polytechnic University, China. His research focuses on thin film encapsulation and organic light-emitting diodes.



**Yu Duan** received his Ph.D. in microelectronics and solidstate electronics from the Jilin University of 2006 under the supervision of Prof. Shiyong Liu. He received his postdoctoral training in the National Nanotechnology Laboratory of CNRINFM (2007–2010) working under Prof. Giuseppe Gigli. He is presently a Professor at the State Key Laboratory on Integrated Optoelectronics, College of Electronic Science and Engineering, Jilin University.